Microstructure and texture evolution in polycrystalline ice during hot torsion. Impact of intragranular strain and recrystallization processes.

Baptiste Journaux[1,2], Thomas Chauve[2,3], Maurine Montagnat[2], Andrea Tommasi[4], Fabrice Barou[4], David Mainprice[4], and Léa Gest[2]

[1]NASA Astrobiology Institute, Department of Earth and Space Sciences, University of Washington, Seattle, USA
[2]Université Grenoble Alpes, CNRS, IRD, G-INP, IGE, F-38000 Grenoble, France
[3]PGP, Department of Geoscience, University of Oslo, Norway
[4]Géosciences Montpellier, Université de Montpellier/CNRS, F-34095 Montpellier, France

Correspondence: Baptiste Journaux (baptiste.journaux@gmail.com), Maurine Montagnat
(maurine.montagnat@univ-grenoble-alpes.fr)

Abstract.

Torsion experiments were performed in polycrystalline ice at high temperature ($0.97 \cdot T_m$) to reproduce simple shear conditions close to those encountered in ice streams and at the base of fast flowing glaciers. As well documented more than 30 years ago (Hudleston, 1977; Bouchez and Duval, 1982), under simple shear ice develops a two-maxima c-axis texture, which evolves

5   rapidly into a single cluster texture with c-axis perpendicular to the shear plane. This evolution still lacks a physical explanation. Current viscoplastic modeling approaches on ice involving dislocation slip on multiple slip systems (basal pyramidal, and prismatic) fail to reproduce it. Dynamic recrystallization mechanisms that occur in both laboratory conditions and in natural setups are likely candidates to explain the texture evolution observed. In this study, we use Electron BackScattering Diffraction (EBSD) and Automatic Ice Texture Analyzer (AITA) to characterize the mechanisms accommodating deformation, the stress

10   and strain heterogeneities that form under torsion of an initially isotropic polycrystalline ice sample at high temperature, and the role of dynamic recrystallization in accommodating these heterogeneities. These analyses highlight an interlocking microstructure, which results from heterogeneity-driven serrated grain boundary migration, and sub-grain boundaries composed by dislocations with [c]-component Burgers vector, indicating that strong local stress heterogeneity develops, even at high temperature and high finite shear strain. Based on these observations, we propose that that nucleation by bulging, assisted by

15   sub-grain boundary formation, is a very likely candidate to explain the progressive disappearance of the texture cluster at low angle to the shear plane and the stability of the one normal to it. We therefore strongly support the development of new models limiting dislocation slip on non-basal slip system and allowing for efficient polygonization by an association of bulging and formation of sub-grain boundaries with a significant [c]-component.

1 Introduction

Ice deforms by shear in many natural conditions such as glaciers and ice sheets, and in particular along ice streams. In most of the deep ice cores studied, compression and extension are the dominant deformation mechanisms owing to the cores location close to geographical domes or along ridges. Simple shear occurs in the deeper portions of these cores, but it is stronger

5 along fast flowing glaciers and ice streams (see review by Hudleston (2015)). During large scale ice flow, deformation induces development of strong crystallographic preferred orientations (CPO) or texture. Since the late 70's a growing number of studies have provided measurements of increasing accuracy of the texture evolution along ice cores (refer to Gow and Williamson (1976); Alley (1988); Lipenkov et al. (1989) for pioneer work, and Faria et al. (2014b) for a review). Pioneer work of Hudleston (1977) analyzed the texture evolution in a narrow shear zone of the Barnes Ice Cap (Canada), providing a well-documented

10 observation of texture development owing to shear in natural conditions. Mantle rocks also develop strong olivine textures, due to deformation and dynamic recrystallization (cf. reviews by Ismaïl and Mainprice (1998); Tommasi and Vauchez (2015)). These textures give rise to anisotropy of both elastic and viscoplastic properties. The former is sampled in the mantle by seismic waves (seismic anisotropy) and the latter plays an important role in the development of plate boundaries (Tommasi et al., 2009) and in basal ice folding, for instance (see e.g. Dahl-Jensen et al. (1997); Thorsteinsson and Waddington (2002); Bons et al.

15 (2016)).

Texture development in ice is related to the strong viscoplastic anisotropy of this material (Alley, 1992). Ice Ih is hexagonal with Space group $P6_3/mmc$, No.194 and Laue class 6/mmm. Plastic strain in ice Ih is mainly accommodated at high temperature by dislocation glide on the basal plane through three 1/3 $<11\bar{2}0>(0001)$ equivalent slip systems (Duval et al., 1983; Hondoh, 2000). The viscoplastic anisotropy of the ice crystal results in strong strain heterogeneities at the inter and

20 intra-granular scale when polycrystalline ice is submitted to a macroscopic stress (Duval et al., 1983; Grennerat et al., 2012) (and reference therein) and hence in activation of dynamic recrystallization processes, even at very low strains (Duval, 1979; Duval et al., 1983; De La Chapelle et al., 1998; Chauve et al., 2017a).

In return, the texture-induced anisotropy at the macro-scale leads to a bulk anisotropic viscosity of ice that impacts ice rheology. This macro-scale mechanical anisotropy is responsible for modifications in ice stratigraphy and age-depth relationship

25 (see e.g. (Martín et al., 2009; Buiron et al., 2011)). It may also produce large scale flow heterogeneities, such as basal folding (see e.g. Dahl-Jensen et al. (1997); Gillet-Chaulet et al. (2006); Ma et al. (2010)). In the case of simple shear the evolution of texture can increase the shear strain by a factor of ten at constant stress (Cuffey and Paterson, 2010; Hudleston, 2015).

In addition to the obvious implications of ice rheology studies to ice caps and glaciers dynamics, ice is also often used as a reference material to study anisotropic mechanical behaviors in rocks and alloys. Since ductile deformation experiments in

30 rocks are challenging, ice is a good analogue to polycrystalline geo-materials for which "high temperature" deformation can be achieved in a cold room and ambient pressure, but at T/T_m close to one. For instance, mantle rocks deformed close to the melting point in the asthenosphere beneath mid-ocean ridges, sampled in ophiolites, display strong olivine texture due to deformation and dynamic recrystallization with fast grain boundary migration (e.g. Cassard et al. (1981); Boudier and

Coleman (1981); Higgie and Tommasi (2012)). The mechanical anisotropy due to these textures may significantly change the flow patterns beneath the ridge (Blackman et al., 2017).

Pioneering experimental studies have shown that at low shear strains ($\gamma < 2$), an initially randomly textured polycrystalline ice sample develops a bimodal distribution of the grains c-axes (Duval, 1981; Bouchez and Duval, 1982). These are noted as

5 the M1 sub-maximum, which remains normal to the macroscopic shear plane, and the M2 sub-maximum, which rotates from near parallel to the shear plane towards the M1 maximum with increasing finite shear strain (Bouchez and Duval, 1982). For important shear strains ($\gamma > 2$), only the M1 maximum persists. This orientation corresponds to crystals with their basal planes well oriented for dislocation glide parallel to the shear plane. The vanishing of the M2 maximum has been hypothesized by Bouchez and Duval (1982) to be due to rigid body rotation and to recrystallization of grains unfavorably oriented for slip.

10 Kamb (1972) has suggested that this texture mainly depends on the finite shear strain and is not sensitive to temperature, strain rate, or stress. This hypothesis has been confirmed by the analysis of natural samples deformed at low strain rates and high shear strains in a glacial shear zone (Hudleston, 1977). Surprisingly, the present state of knowledge on the microscopic processes occurring in polycrystalline ice under simple shear deformation is still limited to these data published over 30 years ago (Kamb, 1959, 1972; Duval, 1981; Bouchez and Duval, 1982; Burg et al., 1986).

15 The tools and methods used then to analyze the texture were often manual and highly dependent on the operator experience. Modern analytical tools are automated and more precise. Electron Back-Scattered Diffraction (EBSD) and Automatic Ice Texture Analyzer (AITA) can now provide high spatial and angular resolution quantitative data, enabling a global and statistical study of the processes accommodating strain at the micro-scale. A modern and comprehensive update of the observations of ice deformation in simple shear seems also more and more necessary as the increase of calculation power allows to run mean-

20 field or full-field modeling routinely (see e.g. Montagnat et al. (2014) for a review). These new numerical approaches, aiming at taking into account all strain accommodation mechanisms, require accurate experimental constraints on the microstructure evolution. It is worth noting that these models are still unable to accurately reproduce texture and evolution of polycrystalline ice and minerals under simple shear. For instance, the recent work by Llorens et al. (2017), which includes some recrystallization processes, does not succeed to reproduce the double sub-maximum of the c-axis preferred orientation or the interlocking grain

25 shapes observed in (Bouchez and Duval, 1982).

The complex interplay of dislocation slip system activities, their interactions, and the role of the various mechanisms accommodating the local strain and stress heterogeneities, such as cross-slip, kink-banding, and dynamic recrystallization, is still not or poorly represented in most of the existing modeling approaches, very likely because of the complexity of the interactions between these mechanisms . Concerning the mantle, recently Signorelli and Tommasi (2015) succeeded to reproduce

30 the evolution of olivine CPO in simple shear with a mean-field modeling approach, by making use of a two-level mechanical interaction scheme that integrates the formation of low-angle grain boundaries as expected during dynamic recrystallization.

The present work aims at giving a modern update on our understanding of simple shear in polycrystalline ice by providing a comprehensive description of the emergence and evolution of texture and grain shape fabric in polycrystalline ice during hot torsion experiments. We use state of the art analytical techniques in material analyses: EBSD equipped with a cryostage

35 and an Automatic Ice Texture Analyzer (AITA), to retrieve quantitative data of unprecedented spatial and angular resolution

on crystallographic orientations, grain size, and grain shape fabrics as a function of shear strain. These data then are used to estimate the active dislocation systems and to investigate the role of sub-grain scale processes on the recrystallization regime that allows the formation of a new texture and microstructure more favorable to shear strain.

2 Experimental methods

5 **Polycrystalline ice preparation**

Unstrained equiaxial polycrystalline ice was prepared by packing evenly 200 μm sieved ice particles in a mould. The container was sealed and the air contained in the porosity was removed using a primary vacuum rotary vane oil pump. Outgassed water at 0°C was quickly introduced afterwards to fill the porosity. The resulting mush was frozen bottom up at -5°C for 48 hours. To enable a more homogenous grain size and recovery of any small strain accumulated during grain growth, the granular

10 ice cylinders were annealed for at least 120 h at -7°C. This method produces untextured homogenous samples with negligible porosity and $\sim$1.5 mm mean grain size. Ultra pure Milli-Q™ water (18 MΩ·cm) was used for all sample preparations. Cylinders around 35 mm in diameter and 60 mm in height were carved from the granular ice using a lathe located in a -10°C cold room. Specific sample sizes are indicated in Table 1.

Torsion experiments

15 Deformation experiments were performed using a torsion apparatus placed inside a cold room at a temperature of -7±0.5°C (0.97·T_m, with T_m the melting temperature at 0°C). Samples were carefully fixed in the apparatus ensuring no axial load. Straight lines parallel to the rotation axis were traced on the surface to control visually any strain heterogeneity along the cylinder (Fig. 1). The surface of the sample was then coated with silicon grease and wrapped gently with a cellophane foil to ensure negligible loss by sublimation.

20 A constant maximum tangential stress was applied on one side of the sample. We imposed a constant torque M corresponding to a maximum stress τ_{max} between 0.4 and 0.6 MPa (Table 1). The τ_{max} was calculated from the torque M using a stress-strain power law as described in Paterson and Olgaard (2000), with a stress exponent of $n = 3$ (Duval et al., 1983). This value of maximum tangential stress has been chosen because it allows high enough strain rates, while preventing the formation of cracks. The actual torque applied value corresponding to each sample is indicated in Table 1.

25 Macroscopic strain was followed using a Linear Variable Differential Transformer (LVDT) during the primary creep regime (i.e. small strains) and a home-made optical rotary encoder device (5000 ipr) for larger strains (Fig. 1). Maximum macroscopic shear strains γ, the maximum natural extensional strain ε, and the strain rate $\dot{\varepsilon}$, calculated through $\varepsilon = \ln \sqrt{\frac{1}{2} \left(2 + \gamma^2 + \gamma \sqrt{4 + \gamma^2} \right)}$ (Paterson and Olgaard, 2000), are reported in Table 1.

Analytical methods

Texture, microstructure, and sub-grain strain heterogeneity analyses were performed using both AITA and EBSD, as the combination of the two techniques allows the acquisition of a comprehensive dataset. AITA enables the analyses of large samples (up to ~10x10 cm^2), but only recovers the c-axis (optical axis) crystallographic orientations. On the other hand, the EBSD

5 setup used is only capable of mapping smaller ice samples (~1x2 cm^2), but is able to recover the full orientation of the crystal (all crystallographic axes) with an expected angular resolution better than 0.7° (Randle, 1992) and with a practical spatial resolution for ice down to 5 μm . Sections tangential to the experimental cylinders were cut out for both AITA and EBSD analyses. The general geometry of these sections is illustrated in Fig. 2. To provide flat surfaces for AITA thin sections and EBSD samples, the sample sections were microtomed by less than 1 mm, which gives an error on γ_{max} of less than 5 %.

10 AITA has been performed on thin sections typically 300 μm thick, as it is routinely done on ice (Russell-Head and Wilson, 1999; Montagnat et al., 2011; Peternell et al., 2011; Chauve et al., 2015; Wilson et al., 2015). We worked at a spatial resolution of 25 μm and were able to obtain an angular resolution of about $\sim 3°$. All optical texture measurements were operated at -7°C. Grains boundaries (GB) were extracted using the segmentation technique described in Montagnat et al. (2015) from automated grain boundaries using color change detection in AITA maps, and manual corrections based on coherent microstructure shapes

15 and discernible misorientations. All manual corrections are operator dependent, so all analyses have been performed by the first author for consistency. This allowed us to differentiate, with a good level of confidence, sub-grain boundaries (SGB) from grain boundaries, even if optical measurements do not give access to the full crystallographic orientation, as EBSD measurements does. From the extracted skeleton images we derived quantified grain size and shape statistics using the PolyLX Matlab® toolbox developed by Lexa (2003). From the grain shapes, we calculated the PARIS grain shape factor to quantify interlocking

20 (angularity). It is defined by PARIS = 2·(P-PE)/PE*100%, with P the perimeter and PE the convex hull perimeter (Heilbronner and Barrett, 2014). This parameter increases with increasing grain boundary sinuosity.

Electron backscattered diffraction (EBSD) patterns were obtained with a CamScan X500FE CrystalProbe equipped with a liquid Nitrogen cryogenic stage (GATAN®) at Geosciences Montpellier (France). Samples surfaces were prepared by carefully flattening the surface with a microtome blade in a -60°C freezer just before loading it on the cold stage. This method provides

25 a very good surface finish and limits to a minimum the heat transfer to the sample, ensuring limited microstructure evolution due to annealing. The CrystalProbe-EBSD working conditions were 15 kV, 3.5 nA, and low vacuum with 1 Pa of gaseous Nitrogen and 25 mm working distance. More details on the EBSD geometry can be found in Demouchy et al. (2011). To avoid ice samples sublimation in the vacuum chamber, which happens at -60.6°C at 1 Pa for ice Ih (Fernicola et al., 2011), the temperature of the cold stage was kept at $-100 \pm 10°$C during the analyses. EBSD Kikuchi patterns were automatically

30 indexed using the HKL Channel5™ software suite (Oxford Instruments®). Maps were acquired with a spatial resolution of 25 μm as it was identify as a good balance between resolution and time constrains, with an indexation rate higher than 85%. Analyses of the EBSD maps were made using the MTEX Matlab® toolbox (Hielscher and Schaeben, 2008; Bachmann et al., 2010, 2011; Mainprice et al., 2014).

To observe the geometry of sub-grain boundaries and extract statistical quantities, local misorientation analyses, such as Kernel average misorientation (KAM) or the local misorientation relative to the mean orientation (Mis2Mean), are usually performed on EBSD data (see review by Wright et al., 2011). Both analyses enable a visualization of the spatial distribution of intragranular stored strain structures, generally in the form of sub-grain boundaries (Wright et al., 2011), but do not provide

5 any information about the type of dislocations accommodating the observed misorientation. On the other hand, the Weighted Burgers Vector (WBV) analysis allows to extract a minimum value for the dislocation density in sub-grain boundaries and provides an estimate of the slip systems necessary to explain the observed misorientations (Wheeler et al., 2009). As conventional EBSD maps are 2D, only 5 components of the Nye tensor α can be extracted ($\alpha_{12}, \alpha_{21}, \alpha_{13}, \alpha_{23}, \alpha_{33}$). This allows to obtain a projection of the Nye tensor on the EBSD map plane which constrain partially the Burgers vector. Hence it provides

10 a lower bound for the dislocation density and the type of dislocations involved in the geometrically necessary dislocations (GND) accommodating the observed misorientations. Even if WBV analysis does not recover the full Burger vectors coordinates, it does not provide "false" components. This means that if a $[c]$-component is measured from WBV analysis of a 2D EBSD map, then the true Burgers vector does actually contains at least this amount of $[c]$-component. For the WBV analysis we used the Matlab® toolbox developed by Wheeler et al. (2009) and previously used on ice in Chauve et al. (2017b).

15 To provide the relative amount of $[c]$-component, the calculated WBV for each pixel is projected on the non-independent 4 hexagonal lattice directions ($[11\bar{2}0]$, $[\bar{2}110]$, $[1\bar{2}10]$, $[0001]$), respectively called WBV_{a1}, WBV_{a2}, WBV_{a3} and WBV_c. The ratio of $[c]$-component (WBV_c) is then given by the relation $rWBV_c = (|WBV_c|/||\text{WBV}||)$, with $||\text{WBV}||$ the Euclidian norm of the WBV. A high-pass value of $0.4°$ ($||\text{WBV}|| > 2.8 \cdot 10^{-4} \mu m^{-1}$) was imposed for the misorientation analysis to filter the noise resulting from the angular resolution of the EBSD data. We suggest to the interested readers to refer the to Appendix

20 A of Chauve et al. (2017b) for more details about this analysis. Nevertheless, it should be reminded that the WBV analysis does not directly provide information about mobile dislocations, responsible for the majority of the plastic deformation. It only measures the GND, as it is based upon the Nye tensor.

3 Results

Five torsion experiments were operated up to different finite shear strains γ_{max}, from 0.012 to 1.94. Details for all experiments

25 are indicated in Table 1. One sample (TGI0.71), with a γ_{max} of 0.71, was annealed for 72 hours at -7° to study the effect of annealing on both texture and microstructure. The microstructure of one of these samples has been partially described in previous work of our team to compare the statistical representation of WBV (or Burger vector) with $[c]$-component in GNDs in samples submitted to uniaxial unconfined compression and to torsion (Chauve et al., 2017b).

Macroscopic strain

30 Retrieved samples presented homogeneous strain with no apparent localization or cracks, as illustrated by the photographs in Fig. 1. TGI0.012 and TGI0.2 shear strain data were very noisy due to signal transmission issues on the acquisition setup, which were fixed for the TGI0.42 and TGI1.96 runs. Typical primary creep regime (i.e. hardening), is observed for TGI0.42 and

TGI1.96 in Fig. 1 until approximately 20,000 s (≈ 6 h).The noise in TGI0.012 and TGI0.2 data was too strong to distinguish any primary creep hardening. After this phase of hardening, a minimum in strain rate is reached (secondary creep regime). This minimum is clearly visible in experiments TGI0.2, TGI0.42, TGI0.71 and TGI1.96 at 200,000 s (≈ 56 h). For the longer TGI1.96 experiment, after the secondary creep phase, strain rate continuously increases until achieving an almost steady state

5 strain rate of $8.5 \cdot 10^{-7}$ s^{-1}, suggesting that tertiary creep regime was reached for this run (Fig. 1). TGI0.012 stayed mostly in the primary creep regime with a $\gamma_{max} = 0.012$. Samples TGI0.2 and TGI0.42 experienced a maximum shear strain of 0.2 and 0.42 respectively. The final strain rate for these two experiments is illustrated by the tangent dashed line in Fig. 1 which shows that softening was still occurring when the samples were unloaded (only the last data points lies on the tangent). We therefore consider that those experiments where still in a transient regime when stopped. A strain step is visible for TGI0.42 between

10 550,000 s (≈ 153 h) and 650,000 s (≈ 180 h) ; it corresponds to a period where the weight used to apply constant torque was in contact with the metallic frame of the torsion apparatus, consequently decreasing the applied stress. After 650,000 s (≈ 180 h), the weight was put back in a good configuration and the strain curve recovered its pre-step slope. The general variation in strain rate evolution with time between the different runs is due to the variability in grain size and textures in the starting material, slightly different sample sizes, and variations in the applied torque (Table 1).

15 **Microstructure evolution**

AITA maps of tangential sections for each sample and associated analyses are presented in Fig. 2 and Table 2. The evolution of texture, microstructure (grain size and shape) as a function of finite shear strain is clearly visible. The color wheel gives the orientation of the <0001> c-axis. The annealed sample TGI0.71 is discussed separately at the end of this section. As the shear strain increases, the distribution of colors changes from random color toward a predominance of red and blue grains, until the

20 map becomes dominated by red color grains for TGI1.96 (γ_{max}=1.96).

This evolution records the progressive change in orientation of the c-axis with increasing shear strain, displayed as pole figures in Fig. 2b. For the undeformed ice sample (γ_{max}=0) we observe random initial orientations of c-axes with a texture index $J_i = 1.07$. The texture J-index is derived by calculating the second moment of the Euler angles orientation distribution function (ODF) of discrete crystal orientation data (Bunge, 1982), and is commonly use to quantify texture strength in geology

25 and in material science. The strain reached by TGI0.012 sample is not high enough to produce any significant change of its texture. As the strain increases we observe the formation of two sub-maxima, as reported in previous studies (Kamb, 1959, 1972; Duval, 1981; Bouchez and Duval, 1982; Burg et al., 1986), one almost perpendicular to the shear plane (M1) and the other one at high angle (45-90°) from the shear plane (M2) as indicated in Fig. 2. With increasing shear, the maxima M1 and M2 increase and decrease in intensity, respectively. This evolution towards a single maximum CPO results in an increase of

30 the J-index (Fig.3). The plane containing the finite extension direction (ED) and normal to the compression direction (CD) has a very low [c]-axis CPO density for $\gamma \geq 0.2$. One should note that for $0.2 \leq \gamma \leq 0.42$, the bimodal pattern formed by the two M1 and M2 submaxima seems to be symmetric relatively to the maximum finite stretching axis. With increasing shear strain the angle between M1 and M2 decreases, but the symmetry is maintained.
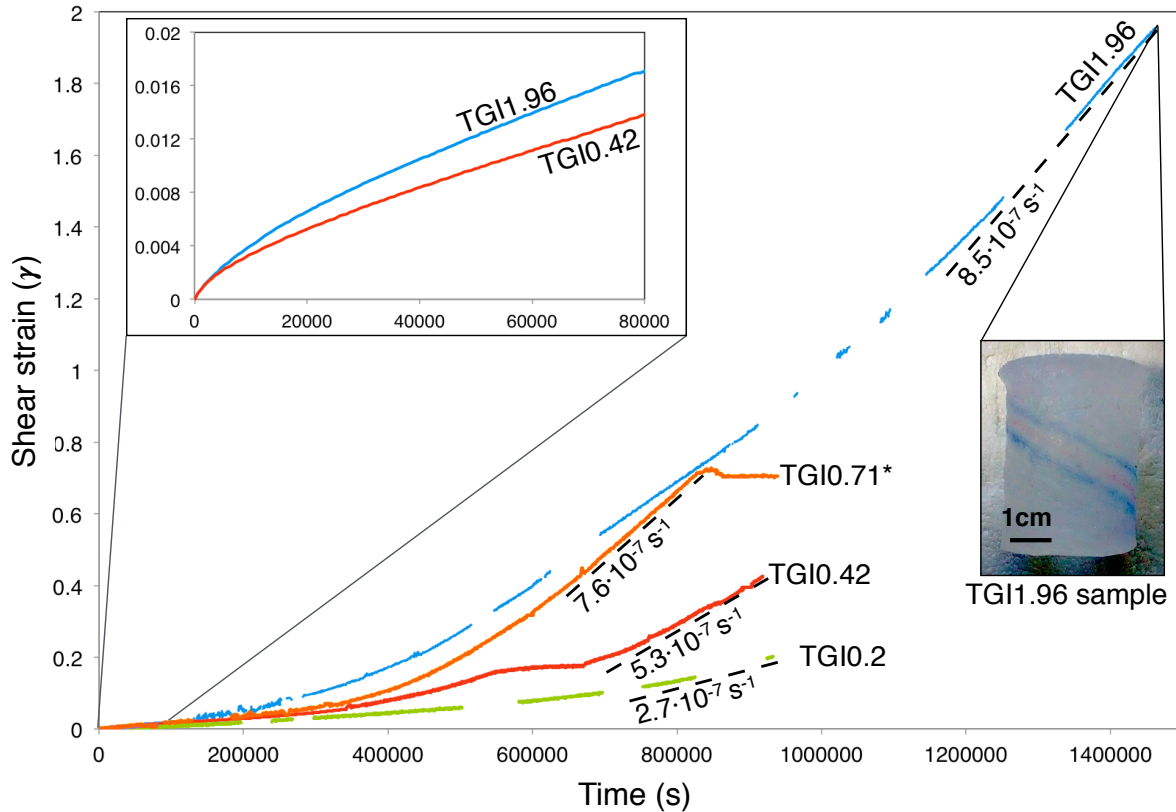
Figure 1. Creep curve for every experiments with the tangent to end of curve as black dashed lines, and corresponding final strain rate $\dot{\varepsilon}_f$. The blank part of the curve corresponds to a loss of signal between the acquisition setup and the sensor located in the cold room. In the top left frame is represented a zoom on the primary creep regime (< 10 h) for better readability. The photograph in the bottom right shows the TGI1.96 sample after unloading, with the inclined ink color stripes, initially straight, used as strain markers.

AITA extracted grain statistics are presented in Table 2. With increasing γ the median grain size diminishes from 0.7(4) mm to 0.12(16)mm. The median is preferred relative to the mean because of the non-normal distribution of grain sizes. The coarser grain size in TGI0.42 sample compared to TGI0.2 and TGI0.012 is probably due to a difference in the initial unstrained grain size, but the grain sizes remain comparable if interquartile ranges are considered. Grain shape fabrics were calculated

5   using moment-based ellipse fitting technics (Lexa, 2003), results are illustrated as rose diagrams in Fig. 2c. As the shear strain increases, we observe the development of a grain shape fabric following the maximum finite elongation direction indicated with the corresponding overlying strain ellipse in Fig. 2.c. The grain shape fabric clearly evolves until $\gamma = 0.42$ and then does not vary significantly up to $\gamma = 1.96$
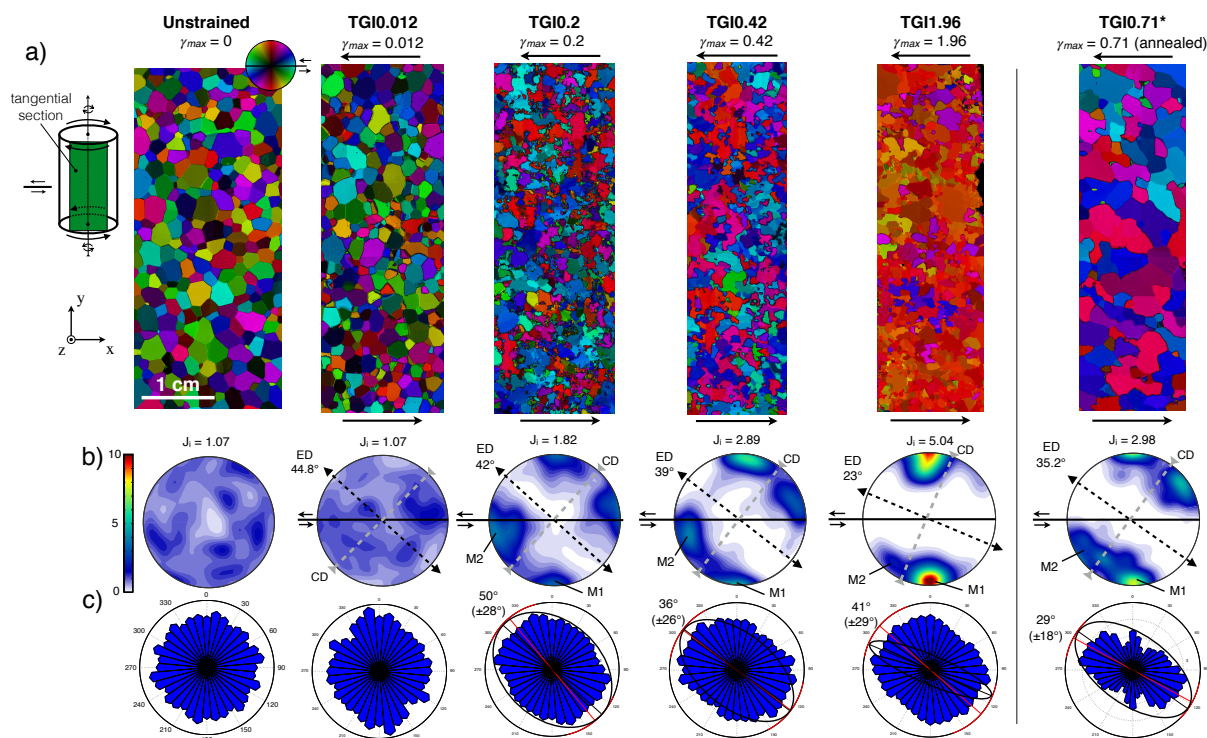
Figure 2. a) AITA analyses of tangential sections for every sample showing the evolution of texture and microstructure, with x parallel to the shear plane and y parallel to the torsion axis. The scheme on the upper right shows the geometrical relation between the tangential section and the retrieved cylindrical samples. Arrows indicate the shear directions. Color-coded c-axis orientation is indicated by the color wheel. b) Pole figures at the bottom show the texture (c-axis orientations) evolution with shear strain with J-index (Bunge, 1982) indicated above. Shear direction, direction of finite extension (ED) and compression direction (CD) are indicated with a black line, doted black line and grey dashed line, respectively. c) Rose diagram of grain shape fabrics. Mean orientation is indicated in red line and 95% confidence interval as a red arc. Finite shear strain ellipses are plotted onto each rose diagram.

Grain boundary interlocking estimated through the PARIS factor (reported in Table 2), seems to increase during the transient strain regime (from 2.2 % at $\gamma = 0$ to 11.5 % at $\gamma = 0.42$). It seems to decrease at a high shear strains of $\gamma = 1.96$ (PARIS = 5.9 %).

The annealed sample TGI0.71 shows a median grain size of 1.7 mm, above the initial unstrained value of 0.7 (Table 2). The
5   CPO seems not modified by the annealing with the M1 and M2 maxima maintained and a J-index = 2.96, which lies in between the values for γ_{max} 0.42 and 1.96, as would be expected from a non-annealed sample with the same finite shear strain (Fig. 2b). The grain shape fabric in the annealed sample is nevertheless more marked than in the strained, but non-annealed samples. The PARIS factor decreases significantly, as much of the interlocking of grains is smoothed by annealing.

As a summary, the crystallographic orientation evolution during simple shear strain of polycrystalline ice can be described
10   from our data as follows. M1 orientations rapidly develop ($\gamma = 0.2$) and increase in intensity until they become predominant
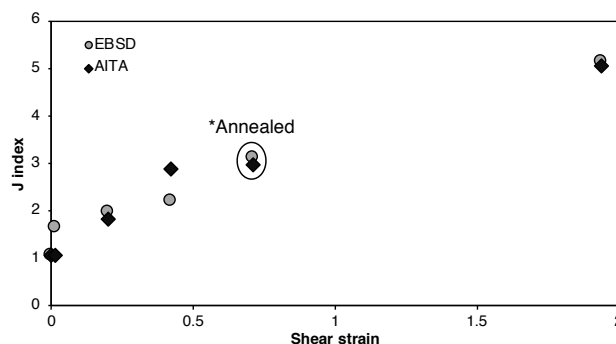
The Cryosphere
Discussions

Figure 3. Texture index J_i determined from AITA and EBSD data for all the shear strains investigated. Annealed sample TGI0.71 is reported for clarity.

at high strains ($\gamma > 1.96$). The M2 maximum also rapidly develops symmetrically to M1 respectively to the maximum finite strain direction. However the M2 maximum continuously decreases in intensity during the transient regime. The other crystallographic orientations start to disappear as early as $\gamma = 0.2$ and this tendency is accentuated with increasing shear strain. Finally, if annealing processes occurs after the strain stops, the CPO is maintained even if the grain shape fabric and grain size are modified.

EBSD

Maps & textures

Multiple EBSD maps were acquired for every final shear strain. Representatives examples of EBSD maps for each sample are shown in Fig. 4.a, with the number of maps n_m acquired for each γ_{max} indicated at the bottom. Spatial resolution is of 25μm. The access to the full crystallographic orientations allows to perform accurate grain segmentation based on misorientation data. Grain boundaries are characterized by misorientations $\geq 5°$ and subgrain boundaries between $1°$ and $5°$ Chauve et al. (2017b)).

The orientations of $<0001>$ $<10\bar{1}0>$ and $<11\bar{2}0>$ axes relatively to the shear plane and direction are shown in Fig. 4.b. All maps acquired for each γ_{max} were combined for better statistical analysis. An excellent level of agreement with CPOs from AITA is observed for $<0001>$ textures, which develop rapidly M1 and M2 sub-maxima, with disappearance of the M2 maximum and reinforcement of the M1 one at high shear strain. The increase in texture J-index confirms this evolution, with very consistent values with those based on the AITA measurements for a same γ_{max} (Fig. 3). Crystallographic orientations of $<10\bar{1}0>$ and $<11\bar{2}0>$ both evolve during strain, until they form a girdle along the macroscopic shear plane at γ_{max}=1.96. We do not observe a significant difference in orientation between $<10\bar{1}0>$ and $<11\bar{2}0>$ at any shear strain.
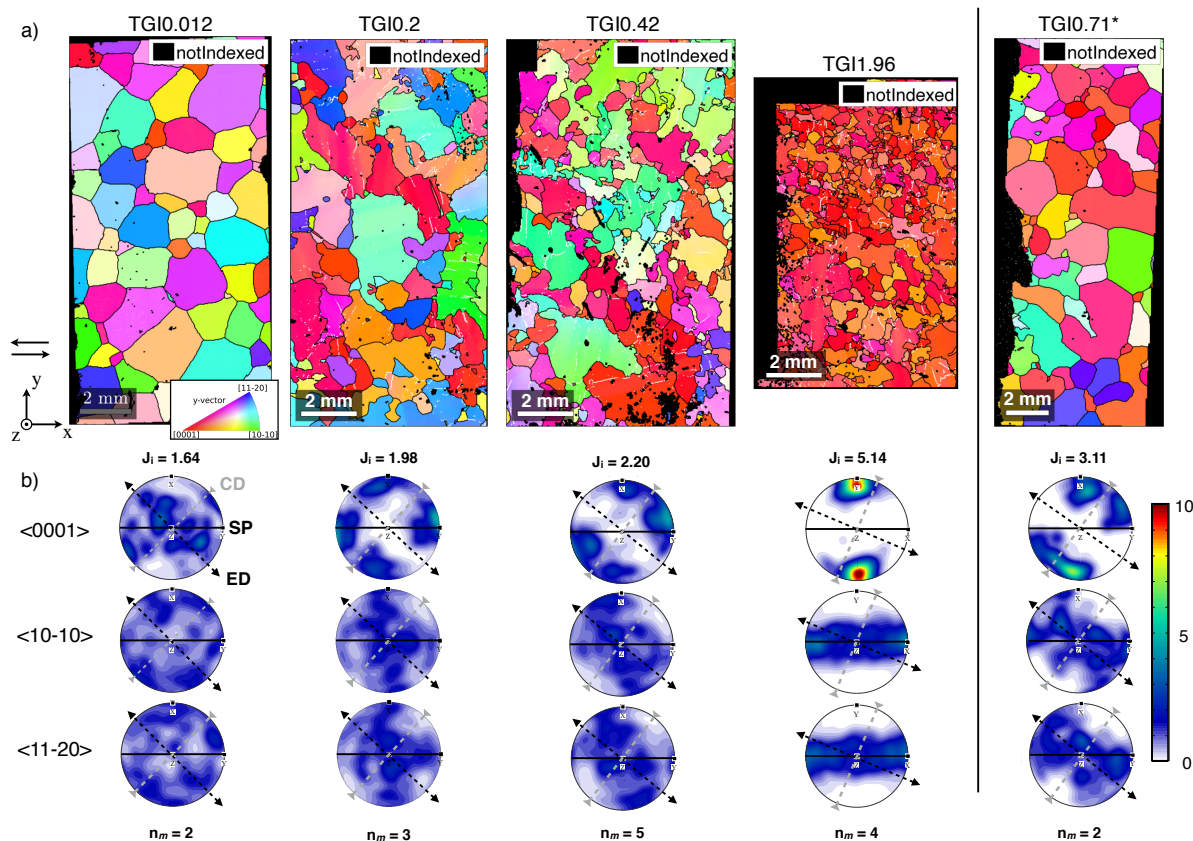
Figure 4. a) Example of EBSD patterns obtained from tangential sections for each maximal shear strain, at -7°C. Map colors correspond to the orientation of the crystallographic lattice toward to the y-axis (torsion axis), as indicated in the inverse pole figure on TGI0.012 EBSD map (top left). Red grains have $\langle 0001 \rangle$ (c-axis) parallel to the torsion axis, green grains have $\langle 10\bar{1}0 \rangle$ (a-axis) parallel to the torsion axis, and blue grains $\langle 11\bar{2}0 \rangle$ (m-axis). Boundaries with misorientation greater than $5°$ are represented in black lines and boundaries between $1°$ and $5°$ are depicted as white lines. b) Lower hemisphere pole figures representing the orientations of $\langle 0001 \rangle$, $\langle 10\bar{1}0 \rangle$ and $\langle 11\bar{2}0 \rangle$ directions of the EBSD data were combined for each γ_{max}. Associated texture J-index is indicated above the pole figure. The shear plane (SP) is indicated as a black line, and the finite extension (ED) and compression (CD) directions, by a black and grey dashed line, respectively. The number of maps used to obtain the pole figures is indicated as n_m.
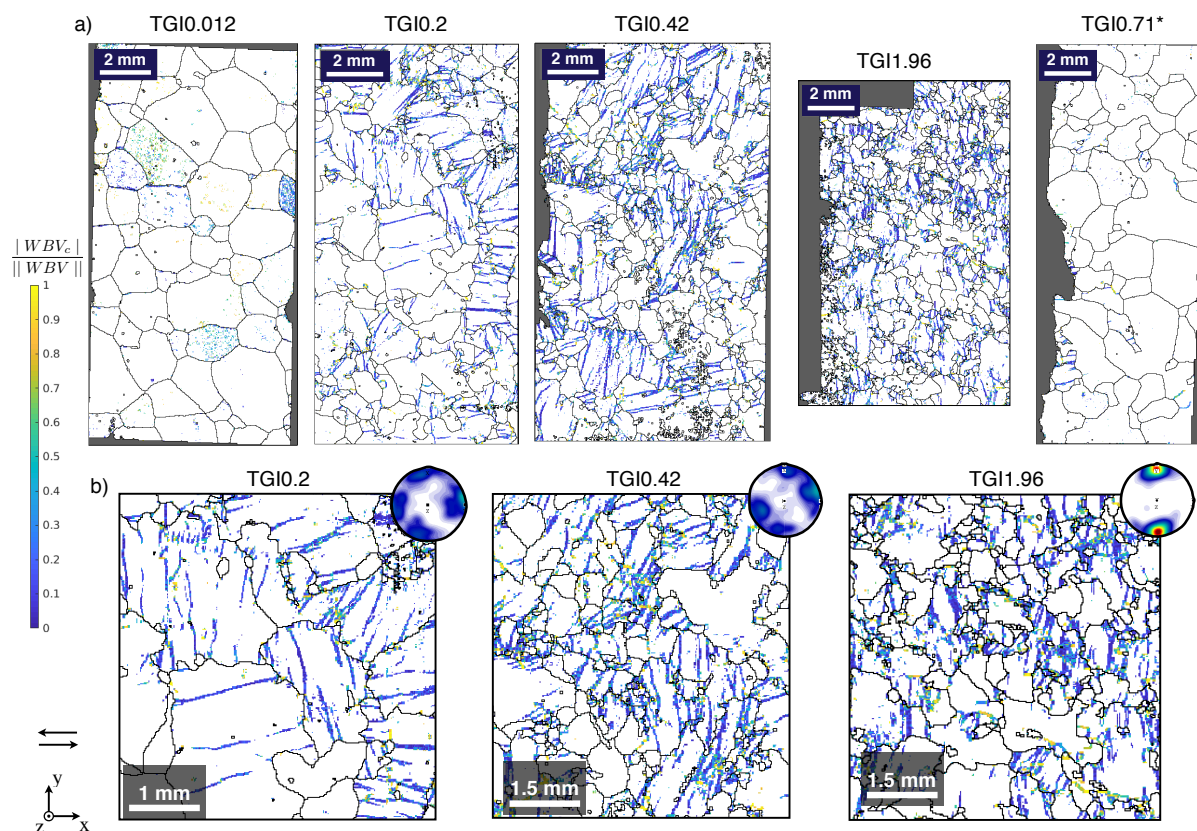
11

Figure 5. Maps of the norm of the Weighted Burgers Vector, ||WBV||. a) Map examples for every shear strain. b) Details on the TGI0.2, TGI0.42 and TGI1.96. Grains boundaries ($> 5°$) are reported as black lines. Non-indexed regions reported in grey

Weighted Burgers Vector analysis and intra-granular strain

During plastic strain, some of the stress on the ice lattice is relieved by the formation and glide of dislocations. Some of those are trapped in the crystal lattice, forming stable arrays of geometrically necessary dislocations (GND), which may define sub-grain boundaries. Such intragranular strain heterogeneities are observed in numerous experimental studies on polycrystalline ice and in natural environments, (Wilson et al., 1986; Mansuy et al., 2000; Piazolo et al., 2008; Montagnat et al., 2011; Weikusat et al., 2011; Faria et al., 2014a; Chauve et al., 2017b). As described in the methods section, WBV analysis allows to derive from intragranular misorientation maps the accumulation of GNDs and to define the relative proportion of dislocations with $< a >$ and $[c]$-component Burgers vector within GNDs. Figure 5 provides representative ||WBV|| maps at every finite shear strain.

In these WBV maps (Fig. 5) we observe a large number of linear sub-grain boundaries already developed at $\gamma_{max} = 0.2$. Evolution of the GNDs density with increasing strain is hard to assess by comparing visually the maps for TGI0.42 and TGI1.96, but it can be assessed by the analysis of the quantitative statistical distribution of $< a >$ and $[c]$ GNDs (Fig. 6).

The sub-grain boundaries are mostly organized in walls and the direction of the trace of these planes on the thin section typically corresponds to the parent grain $[c]$-axis direction. This kind of sub-grain boundaries, very common in both natural and experimentally deformed ice, has been previously identify as basal tilt boundaries composed of basal edge dislocations ($b = a$, with b the Burgers vector) through EBSD and X-Ray Laue diffraction (Piazolo et al., 2008; Weikusat et al., 2011;

5   Chauve et al., 2017b). These sub-grain boundaries are visible in Fig. 5b as purple and blue lines. Other kind of low angle boundaries were also identified in both natural and experimentally deformed ice; these are basal twist boundaries with basal screw dislocation and non-basal tilt boundaries with variable amounts of dislocations with $[c]$ axis Burgers vector component (i.e. $< a+c >$ and $[c]$) (Piazolo et al., 2008; Weikusat et al., 2011; Piazolo et al., 2015; Chauve et al., 2017b). Such sub-boundaries are also identified in the present study (green to yellow lines in Fig. 5b) It is interesting to note that even the most

10   deformed sample, which has a strong CPO with one single sub-maxima at $\gamma_{max} = 1.96$ (at steady state tertiary creep), GNDs are very common. In the almost undeformed (TGI0.012) and annealed cases (TGI0.71), almost no sub-grain boundaries are identifiable.

As demonstrated by Chauve et al. (2017b), the total density of GNDs with a significant $||WBV||$ clearly increases with shear strain (Fig. 6f). However, the ratio of $[c]$-component ($rWBV_c = |WBV_c|/||WBV||$) of GNDs remains constant at ca. 35 %

15   ($rWBV_c > 1/3$, or $< a+c > + [c]$). For the lowest shear strain (TGI0.012) the $[c]$-component ratio is larger, but this could be due to the lower statistics, as t the density of GNDs (i.e. nb of pixels with a $||WBV|| > 2.8 \cdot 10^{-4}$ μm^{-1}) is much lower. By classifying grains by orientation, it is possible to look at the individual statistics for the grains composing the M1 and the M2 maxima and in other orientations (Fig. 6a to 6e). By looking at the pixel orientation statistic, it seems that the proportion of M2 pixels rapidly increases compared to M1 at $\gamma_{max} = 0.2$, and then gradually decreases at $\gamma_{max} = 0.42$, eventually disappearing at

20   $\gamma_{max} = 1.96$. When performing the WBV analysis for each grain family, the presence of GNDs with a $[c]$-component Burgers vector does not seem to be correlated with the orientation of the grain. The only exception is for the annealed case at $\gamma_{max} = 0.71$, where recovery processes and noise due to poor statistics limit the use of such analysis. This is consistent with previously published data on $[c]$-component GNDs for both shear and compression experiments from Chauve et al. (2017b).

We computed the probability density function of $rWBV_c$ as function of the distance to the grain boundary, and represented it

25   for $rWBV_c < 1/3$, $1/3 < rWBV_c < 2/3$ and $rWBV_c > 2/3$ in Fig. 7. We are able to observe that the $rWBV_c < 1/3$ density clearly decreases around 100 μm close to the grain boundary, when both $2/3 < rWBV_c < 2/3$ and $rWBV_c > 2/3$ densities increases ($rWBV_c > 2/3$ almost doubles). This statistical analysis clearly shows the increase of $[c]$-component dislocations proportion in the substructures at a distance lower than 100 μm from the grain boundary. It is also important to note that we do not observe any significant differences between different finite shear strains.

30   ## 4   Discussion

The present data corroborates the previous observations on the texture evolution in ice deformed by simple shear by Hudleston (1977); Bouchez and Duval (1982), with an important increase in quantitative analysis and pushing the statistical analysis down to the intragranular level.
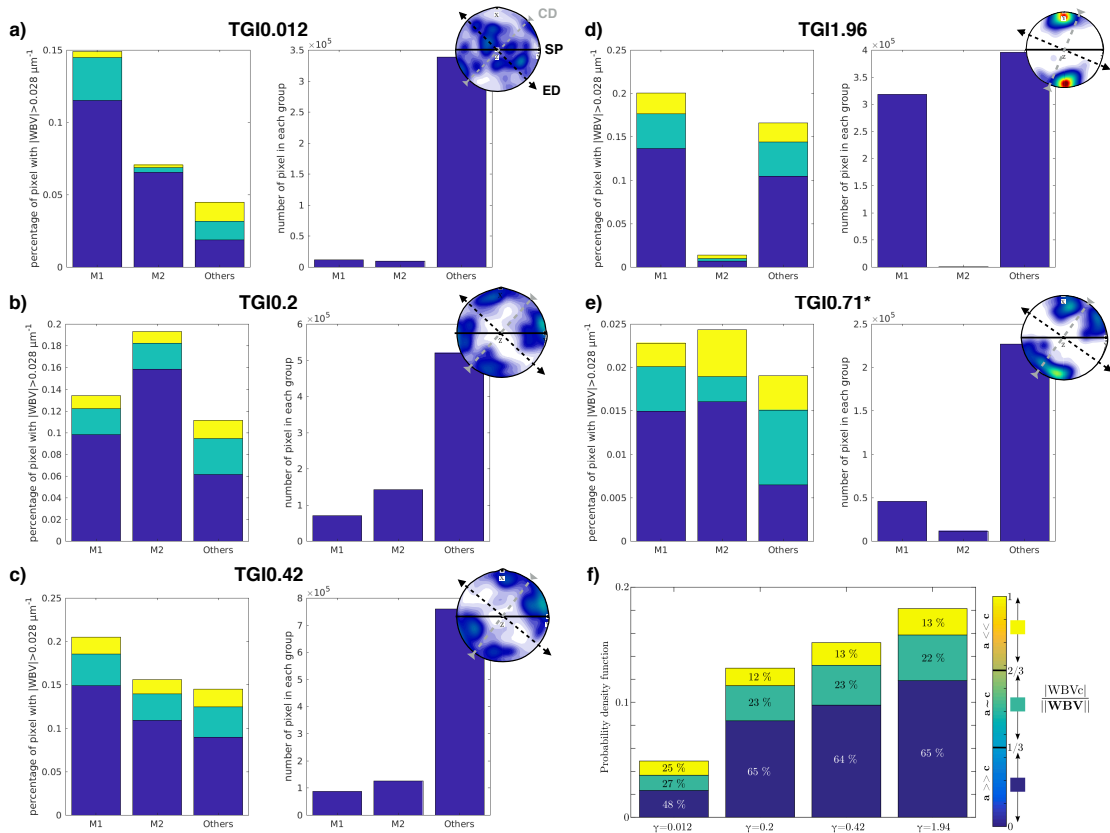
Figure 6. a,b,c,d,e) Statistical distribution of pixels per group of orientation (M1, M2 sub-maxima or other) and per $rWBV_c$ ensemble for each γ_{max} 0.012, 0.2, 0.42, 1.96 and 0.71 respectively, with associated number of pixels per group. The c-axis pole figure is also reported for each finite shear strain at the top right. f) Distribution of pixels with a $||WBV||$ higher than a threshold of $(2.8 \cdot 10^{-4}\ \mu m^{-1})$. Evolution with torsion strain of the relative $[c]$ and $<a>$ components over the norm of the full WBV ($|WBV_c|/||WBV||$) for four distinct torsion creep tests. See Chauve et al. (2017b) for more details.

As indicated by the evolution of the macroscopic strain rates on Fig. 1, we were able to analyze the texture and microstructure at different creep regimes. The near constant strain rate ($\dot{\varepsilon}_f = 8.5 \cdot 10^{-7}\mathrm{s}^{-1}$) achieved for the TGI1.96 run can be interpreted as the evidence that this sample was close to steady state in terms of mechanical behavior, typical of tertiary creep regime. The apparition and evolution of c-axis orientation sub-maxima M1 and M2 in the texture are consistent with previous data from Hudleston (1977) and Bouchez and Duval (1982). The M1 maximum remains always normal to the shear plane and the M2 sub-maximum, initially as strong as M1, progressively rotates with shear during transient creep, and decreases in intensity until it disappears, possibly as tertiary creep regime is reached.

The slow evolution of the grain shape preferred orientations and their saturation at shear strains higher than 0.2, visible from the grain shape orientation rose diagram (Fig. 2.c), could be the effect of recrystallization processes and fast grain boundary

The Cryosphere
Discussions

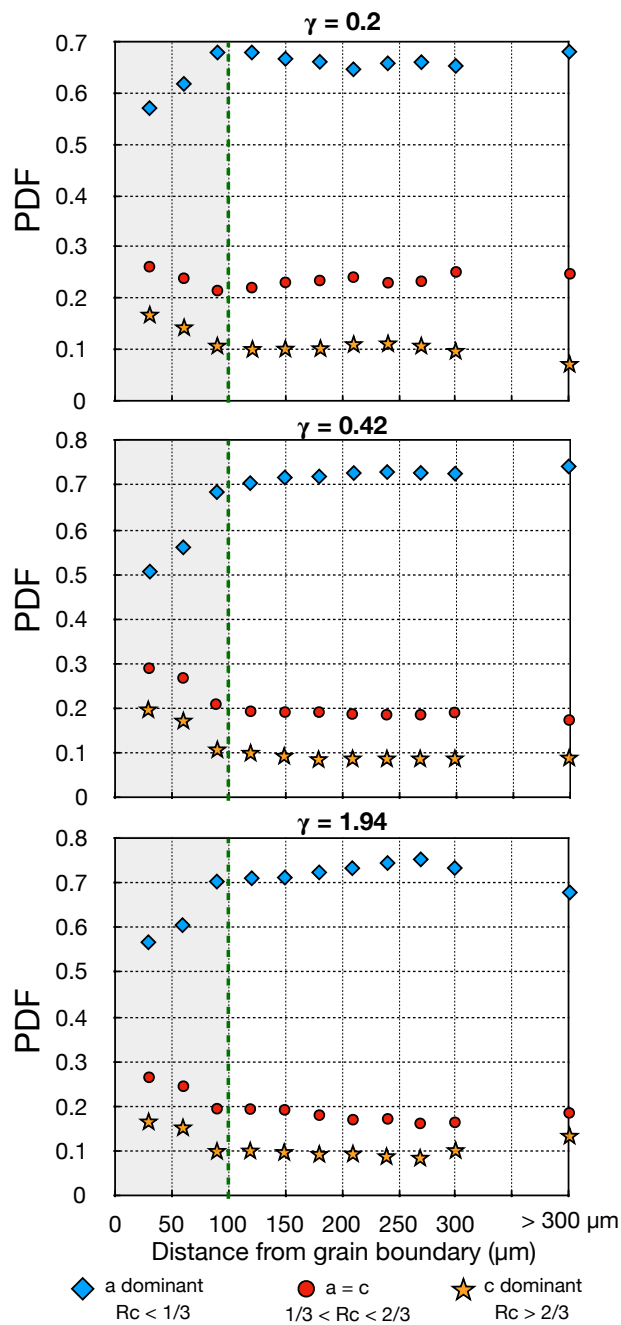**Figure 7.** Probability density function for $rWBV_c < 1/3$ (blue diamonds), $2/3 < rWBV_c < 2/3$ (red circles) and $rWBV_c > 2/3$ (yellow stars) components of the GNDs across profiles from grain boundaries to cores of the GNDs, extracted from WBV maps, for TGI0.2, TGI0.42 and TGI1.96. The green dotted line represents the 100 μm distance to the grain boundary.

migration that counters the formation of a strong grain shape fabric. These processes may also explain why we observe a decrease in the grain boundary interlocking at high strains and even in the annealed sample through the PARIS factor (Table 2). Indeed nucleation should enable the apparition and growth of new grains with small PARIS factors at the expenses of older grains with serrated grain boundaries (i.e. higher PARIS). This observation underlines that the estimation of strain magnitude

5   from grain elongation or shape is not reliable at high temperature, as noted by Burg et al. (1986). The efficiency of grain boundary migration and recovery of shape fabric is expected to significantly decrease with decreasing temperatures. The case of the annealed sample TGI0.71 is interesting to understand how metadynamic annealing processes like grain boundary migration driven by dislocation density variation may change the microstructure and texture (CPO). The texture is maintained, the grain shape fabric is reinforced, and the final grain size is larger than the initial one. The preservation of the texture suggests that

10 most new "dislocation free" nucleii were already close to M1 or M2 orientations. This would favor predominance of nucleation by bulging over spontaneous nucleation, as the later tends to produce random orientations (Chauve et al., 2017a). This also means that if stress is somehow lowered in natural context, and annealing takes place, the texture could still be interpreted, even if information about grain shape fabric is lost. The reinforcement of the grain shape fabric visible on the rose diagram in Fig. 2.c also suggests some oriented grain growth. It is possible that during strain, the formation of a large number of isometric

15 nucleii weakens the shape fabric, but that this signal is erased during static annealing.

The full lattice preferred orientations derived from EBSD data reveal that neither $<10\bar{1}0>$ nor $<11\bar{2}0>$ axes display any preferential orientation within the shear plane, even at high shear strain ($\gamma = 1.96$, Fig. 4). This corresponds to an isotropic plastic response on the basal plane during simple shear strain in polycrystalline ice. 1/3 $<11\bar{2}0>$(0001) slip systems are supposed to be dominant in the basal plane (Hondoh, 2000); this assumption is consistent with the present data, but glide in

20 the $<10\bar{1}0>$ direction is also possible.

From WBV analysis of the EBSD maps, we were able to map GNDs and obtain information about their Burgers vectors components. If the density of GNDs increases with shear strain, the amount of GNDs with Burgers Vector with a $[c]$-component seems to be independent of the amount of deformation. However there is a clear increase of the amount of GNDs with a $[c]$-component Burgers vector in the vicinity of the grain boundaries, as illustrated on Fig. 7. The increase of GNDs with a higher

25 density of $[c]$-component Burgers vector, predicted to be unfavorable compared to basal plane dislocations, is probably due to accommodation of strong local stresses different from the macroscopic one, close to GBs. As pointed out by Chauve et al. (2017a), there is a clear connection between the nucleation bulging mechanisms and GNDs near serrated grain boundaries. There have been also direct observations of GND loops in ice that require $[c]$-component dislocation walls to be closed (Chauve et al., 2017b). This would suggest that the increase of $[c]$-component GNDs near grain boundary helps to form GND loops that

30 give birth to new nucleii. These observations, combined with our present WBV statistical analysis, point towards a possible way to estimate the maximum size of bulging nucleus, which would be lower than 100 μm in the present case. It would be important in future studies to test if this critical dimension would vary with temperature or stress, as well as to obtain misorientation data at higher spatial resolution to better constrain the evolution of this higher $[c]$-component dislocation zone. The fact that the possible maximum size of bulging nucleus is constant at all finite shear strains suggests that bulging is very active at all creep

35 regime, further stressing its importance for understanding the rheology of ice and other materials at high temperatures.

Our experimental results and the ones of Bouchez and Duval (1982) are in general disagreement with modeling of shear in ice either by mean-field approach as in (Wenk et al., 1997) or more recently by full-field modeling as in (Llorens et al., 2017). This later work predicts only one single submaxima inclined from the tangent to the shear plane, and a preferred orientation of $<11\bar{2}0>$ within the shear plane. These models consider that plastic strain from dislocation slip results not only from slip on the basal plane, but also on prismatic and pyramidal planes. By activating these later slip systems, the lattice is geometrically forced to rotate away from the normal to the shear plane, creating unrealistic textures neither M1 nor M2 sub-maxima. On the contrary, pioneering work on 2D modeling of polycrystalline aggregates under simple shear by Etchecopar (1977) was able to reproduce the 2 sub-maxima M1 and M2. This was simply done by considering a single slip system (basal slip system for ice) and allowing cells to subdivide (polygonization) and undergo rigid body rotation. The very good agreement of this simple model with evolution of textures observed experimentally for ice under shear was emphasized by Bouchez and Duval (1982), who hypothesized that the polygonization processes in ice would be formation of GNDs and kink-bands. In our results few kink bands were observed, but the prevalence of GNDs at most finite shear strains suggests that Bouchez and Duval (1982) supposition is reasonable. Indeed, rotation of the dominant slip system into parallelism with the imposed macroscopic shear is predicted by the mean-field VPSC model modified to account for subgrain rotation recrystallization (Signorelli and Tommasi, 2015). Yet, in these study parallelism is only achieved at shear strains of 5, whereas in the present study and in Bouchez and Duval (1982) a single maximum texture is observed for shear strains as low as 2. This points to an additional contribution to the texture reorientation, which at the high homologous temperatures of both experimental studies might be nucleation by bulging associated with sub-grain rotation as a bulge closure, and fast grain boundary migration.

The analysis of the texture evolution in the experiments suggests that plastic strain through dislocation creep is probably as commonly claimed, largely dominated by basal slip. Nevertheless, stored GNDs (including non-basal GNDs with [c]-component Burgers vector) allow recrystallization accommodation mechanisms such as nucleation by bulging. The fact that the PARIS factor initially increases then decreases above γ_{max} =0.42 enables to make further assumptions about active recrystallization mechanisms and their evolution (or sequence) with increasing strain. Until a strain close to γ_{max} =0.42, heterogeneities in dislocation storage close to grain boundaries favor spatially irregular grain boundary migration to dominate, creating numerous serrated grain boundaries, as indicated by the increasing PARIS factor. With increasing finite strain, the influence of nucleation gradually increases, forming more isodiametric grains, lowering the PARIS factor, and eventually erasing the M2 texture. Indeed, SGBs required to close bulges may necessitate strong local stress levels (in order to activate [c]-component dislocations, for instance) that are obtained after a given amount of accumulated strain, while grain boundary migration may occurs since the very beginning of the deformation.

Our results also underline the efforts remaining to match experimental observations and mean-field and full-field numerical modeling. Comparing our data to Llorens et al. (2017) models, it seems clear that the numerical approach is not able to reproduce the initial 2 sub-maxima, and the later single maxima, normal to the macroscopic shear plane. This could be due to several processes that are not taken into account in the models and that, based on the present data, seem to play an important role, namely the bulging nucleation process and the possibility of non-basal dislocation slip to participate to SGB related polygonisation.

5 Conclusions

By using state of the art analytical techniques (i.e. AITA, EBSD and WBV analysis), we were able to characterize the texture, microstructure, and geometrically necessary dislocation structures in ice deformed under torsion in the laboratory at an unprecedented resolution. The experiments, performed at high temperature and up to shear strain of 2, favored dynamic recrystallization mechanisms, in conditions close to those encountered in cold glaciers, ice stream and even some deep ice core areas. From these high-resolution observations, we were able to highlight the impact of grain boundary migration and nucleation by bulging, associated with sub-grain boundary formation, as the main mechanisms responsible for texture and shape fabric evolution with strain. Sub-grain boundaries density and dislocation components are characterized as abundant at all observed finite shear strain, even at this high temperature ($0.97 \cdot T_m$). Furthermore, around 30% of Geometrically Necessary Dislocations exhibit a significant $[c]$ component, due to strong local stresses arising from the strong viscoplastic anisotropy of the ice crystals. This $[c]$ component increases close to grain boundary, suggesting that this process may efficiently participate to the closing of bulging grain boundary during bulging nucleation.

So far, full-field modeling approaches that simulate plastic deformation by activating non-basal slip systems in ice are unable to reproduce the strongly clustered simple shear texture observed experimentally and in the nature. As was already suggested by Etchecopar (1977), polygonization may play a crucial role to accommodate dislocation glide dominated by basal slip. Our observations suggest that bulging, associated with sub-grain boundaries mechanisms, could be responsible for this and explain the observed strongly clustered texture at relatively high strain and high temperature. We conclude that that non- basal dislocation slip should not be involved in modeling to obtain realistic textures in polycrystalline ice and other anisotropic material, but that GNDs with a $[c]$ components should play a major role in strain accommodation and nucleation processes. We hope that these new results will help the modeling community to provide realistic modeling texture evolution of simple shear in ice, which are capital for a better predictive ability of ice landmasses evolution in the coming decades and centuries.

Code availability. MTEX is a free Matlab® toolbox for analyzing and modeling crystallographic textures by means of EBSD or pole figure data (Hielscher and Schaeben, 2008; Bachmann et al., 2010, 2011; Mainprice et al., 2014). It is available on http://mtex-toolbox.github.io/ The Weighted Burgers Vetctor (WBV) analysis is a Matlab® toolbox developed by Wheeler et al. (2009).
PolyLX is a free MATLAB® toolbox for quantitative analysis of microstructures, developed by Lexa (2003), and available on https://petrol. natur.cuni.cz/~ondro/oldweb/polylx:home

Author contributions. Sample preparation and torsion experiments were performed in Grenoble by BJ and LG. EBSD measurements were operated in Montpellier by BJ, TC, MM, FB, and LG. Data analysis were conducted by BJ and TC. Interpretation was done by BJ, TC, MM, AT and DM. BJ and MM wrote the paper with input from all authors.

References

Alley, R. B.: Fabrics in polar ice sheets: development and prediction, Science (New York, N.Y.), 240, 493–495, https://doi.org/10.1126/science.240.4851.493, 1988.

Alley, R. B.: Flow-law hypotheses for ice-sheet modeling, Journal of Glaciology, 38, 245–256, https://doi.org/10.3189/S0022143000003658, 1992.

Bachmann, F., Hielscher, R., and Schaeben, H.: Texture Analysis with MTEX – Free and Open Source Software Toolbox, Solid State Phenomena, 160, 63–68, https://doi.org/10.4028/www.scientific.net/SSP.160.63, 2010.

Bachmann, F., Hielscher, R., and Schaeben, H.: Grain detection from 2d and 3d EBSD data—Specification of the MTEX algorithm, Ultramicroscopy, 111, 1720–1733, https://doi.org/10.1016/j.ultramic.2011.08.002, 2011.

Blackman, D. K., Boyce, D. E., Castelnau, O., Dawson, P. R., and Laske, G.: Effects of crystal preferred orientation on upper-mantle flow near plate boundaries: rheologic feedbacks and seismic anisotropy, Geophysical Journal International, 210, 1481–1493, https://doi.org/10.1093/gji/ggx251, 2017.

Bons, P. D., Jansen, D., Mundel, F., Bauer, C. C., Binder, T., Eisen, O., Jessell, M. W., Llorens, M.-G., Steinbach, F., Steinhage, D., and Weikusat, I.: Converging flow and anisotropy cause large-scale folding in Greenland's ice sheet, Nature Communications, 7, 11 427, https://doi.org/10.1038/ncomms11427, 2016.

Bouchez, J. l. and Duval, P.: The Fabric of Polycrystalline Ice Deformed in Simple Shear: Experiments in Torsion, Natural Deformation and Geometrical Interpretation, Textures and Microstructures,, 5, 171–190, https://doi.org/10.1155/TSM.5.171, 1982.

Boudier, F. and Coleman, R. G.: Cross section through the peridotite in the Samail Ophiolite, southeastern Oman Mountains, Journal of Geophysical Research: Solid Earth, 86, 2573–2592, https://doi.org/10.1029/JB086iB04p02573, 1981.

Buiron, D., Chappellaz, J., Stenni, B., Frezzotti, M., Baumgartner, M., Capron, E., Landais, A., Lemieux-Dudon, B., Masson-Delmotte, V., Montagnat, M., Parrenin, F., and Schilt, A.: TALDICE-1 age scale of the Talos Dome deep ice core, East Antarctica, Climate of the past, 7, 1–16, https://doi.org/info:doi:10.5194/cp-7-1-2011, 2011.

Bunge, H.-J.: Texture Analysis in Materials Science: Mathematical Methods, Elsevier, butterworth & co edn., 1982.

Burg, J. P., Wilson, C. J. L., and Mitchell, J. C.: Dynamic recrystallization and fabric development during the simple shear deformation of ice, Journal of Structural Geology, 8, 857–870, https://doi.org/10.1016/0191-8141(86)90031-3, 1986.

Cassard, D., Nicolas, A., Rabinovitch, M., Moutte, J., Leblanc, M., and Prinzhofer, A.: Structural classification of chromite pods in southern New Caledonia, Economic Geology, 76, 805–831, https://doi.org/10.2113/gsecongeo.76.4.805, 1981.

Chauve, T., Montagnat, M., and Vacher, P.: Strain field evolution during dynamic recrystallization nucleation; A case study on ice, Acta Materialia, https://doi.org/10.1016/j.actamat.2015.08.033, 2015.

Chauve, T., Montagnat, M., Barou, F., Hidas, K., Tommasi, A., and Mainprice, D.: Investigation of nucleation processes during dynamic recrystallization of ice using cryo-EBSD, Phil. Trans. R. Soc. A, 375, 20150 345, https://doi.org/10.1098/rsta.2015.0345, 2017a.

Chauve, T., Montagnat, M., Piazolo, S., Journaux, B., Wheeler, J., Barou, F., Mainprice, D., and Tommasi, A.: Non-basal dislocations should be accounted for in simulating ice mass flow, Earth and Planetary Science Letters, 473, 247–255, https://doi.org/10.1016/j.epsl.2017.06.020, 2017b.

Cuffey, K. and Paterson, W. S. B.: The Physics of Glaciers, Elsevier, Masterdam, Netherlands, 2010.

Dahl-Jensen, D., Thorsteinsson, T., Alley, R., and Shoji, H.: Flow properties of the ice from the Greenland Ice Core Project ice core: The reason for folds?, Journal of Geophysical Research: Oceans, 102, 26 831–26 840, https://doi.org/10.1029/97JC01266, 1997.

De La Chapelle, S., Castelnau, O., Lipenkov, V., and Duval, P.: Dynamic recrystallization and texture development in ice as revealed by the study of deep ice cores in Antarctica and Greenland, Journal of Geophysical Research: Solid Earth, 103, 5091–5105, https://doi.org/10.1029/97JB02621, 1998.

Demouchy, S., Mainprice, D., Tommasi, A., Couvy, H., Barou, F., Frost, D. J., and Cordier, P.: Forsterite to wadsleyite phase transformation under shear stress and consequences for the Earth's mantle transition zone, Physics of the Earth and Planetary Interiors, 184, 91–104, https://doi.org/10.1016/j.pepi.2010.11.001, 2011.

Duval, P.: Creep and recrystallization of polycrystalline ice, Bulletin de Mineralogie, 102, 80–85, 1979.

Duval, P.: Creep and fabrics of polycrystalline ice under shear and compression, Journal of Glaciology, 27, 129–140, 1981.

Duval, P., Ashby, M. F., and Anderman, I.: Rate-controlling processes in the creep of polycrystalline ice, The Journal of Physical Chemistry, 87, 4066–4074, https://doi.org/10.1021/j100244a014, 1983.

Etchecopar, A.: A plane kinematic model of progressive deformation in a polycrystalline aggregate, Tectonophysics, 39, 121–139, https://doi.org/10.1016/0040-1951(77)90092-0, 1977.

Faria, S. H., Weikusat, I., and Azuma, N.: The microstructure of polar ice. Part II: State of the art, Journal of Structural Geology, 61, 21–49, https://doi.org/10.1016/j.jsg.2013.11.003, 2014a.

Faria, S. H., Weikusat, I., and Azuma, N.: The microstructure of polar ice. Part II: State of the art, Journal of Structural Geology, 61, 21–49, https://doi.org/10.1016/j.jsg.2013.11.003, 2014b.

Fernicola, V., Rosso, L., and Giovannini, M.: Investigation of the Ice–Water Vapor Equilibrium Along the Sublimation Line, International Journal of Thermophysics, 33, 1363–1373, https://doi.org/10.1007/s10765-011-1128-2, 2011.

Gillet-Chaulet, F., Gagliardini, O., Meyssonnier, J., Zwinger, T., and Ruokolainen, J.: Flow-induced anisotropy in polar ice and related ice-sheet flow modelling, Journal of Non-Newtonian Fluid Mechanics, 134, 33–43, https://doi.org/10.1016/j.jnnfm.2005.11.005, 2006.

Gow, A. J. and Williamson, T.: Rheological implications of the internal structure and crystal fabrics of the West Antarctic ice sheet as revealed by deep core drilling at Byrd Station, GSA Bulletin, 87, 1665–1677, https://doi.org/10.1130/0016-7606(1976)87<1665:RIOTIS>2.0.CO;2, 1976.

Grennerat, F., Montagnat, M., Castelnau, O., Vacher, P., Moulinec, H., Suquet, P., and Duval, P.: Experimental characterization of the intra-granular strain field in columnar ice during transient creep, Acta Materialia, 60, 3655–3666, https://doi.org/10.1016/j.actamat.2012.03.025, 2012.

Heilbronner, R. and Barrett, S.: Image Analysis in Earth Sciences, Springer, 2014.

Hielscher, R. and Schaeben, H.: A novel pole figure inversion method: specification of the MTEX algorithm, Journal of Applied Crystallography, 41, 1024–1037, https://doi.org/10.1107/S0021889808030112, 2008.

Higgie, K. and Tommasi, A.: Feedbacks between deformation and melt distribution in the crust–mantle transition zone of the Oman ophiolite, Earth and Planetary Science Letters, 359-360, 61–72, https://doi.org/10.1016/j.epsl.2012.10.003, 2012.

Hondoh, T.: Nature and behavior of dislocations in ice, Physics of Ice Core Records, pp. 3–24, 2000.

Hudleston, P. J.: Progressive Deformation and Development of Fabric Across Zones of Shear in Glacial Ice, in: Energetics of Geological Processes, edited by Saxena, S. K., Bhattacharji, S., Annersten, H., and Stephansson, O., pp. 121–150, Springer Berlin Heidelberg, 1977.

Hudleston, P. J.: Structures and fabrics in glacial ice: A review, Journal of Structural Geology, 81, 1–27, https://doi.org/10.1016/j.jsg.2015.09.003, 2015.

Ismaïl, W. B. and Mainprice, D.: An olivine fabric database: an overview of upper mantle fabrics and seismic anisotropy, Tectonophysics, 296, 145–157, https://doi.org/10.1016/S0040-1951(98)00141-3, 1998.

Kamb, B.: Experimental Recrystallization of Ice Under Stress, in: Flow and Fracture of Rocks, edited by Heard, H. C., Borg, I. Y., Carter, N. L., and Raleigh, C. B., pp. 211–241, American Geophysical Union, 1972.

Kamb, W. B.: Ice petrofabric observations from Blue Glacier, Washington, in relation to theory and experiment, Journal of Geophysical Research, 64, 1891–1909, https://doi.org/10.1029/JZ064i011p01891, 1959.

5 Karato, S., Zhang, S., Zimmerman, M., and Daines, M.: Experimental studies of shear deformation of mantle materials: Towards structural geology of the mantle, Pure and Applied Geophysics, 1998.

Lexa, O.: Numerical approach in structural and microstructural analyses, Ph.D. thesis, Charles University, Prague, Czech Republic, 2003.

Lipenkov, V. Y., Barkov, N. I., Duval, P., and Pimienta, P.: Crystalline Texture of the 2083 m Ice Core at Vostok Station, Antarctica, Journal of Glaciology, 35, 392–398, https://doi.org/10.3189/S0022143000009321, 1989.

10 Llorens, M.-G., Griera, A., Steinbach, F., Bons, P. D., Gomez-Rivas, E., Jansen, D., Roessiger, J., Lebensohn, R. A., and Weikusat, I.: Dynamic recrystallization during deformation of polycrystalline ice: insights from numerical simulations, Phil. Trans. R. Soc. A, 375, 20150 346, https://doi.org/10.1098/rsta.2015.0346, 2017.

Ma, Y., Gagliardini, O., Ritz, C., Gillet-Chaulet, F., Durand, G., and Montagnat, M.: Enhancement factors for grounded ice and ice shelves inferred from an anisotropic ice-flow model, Journal of Glaciology, 56, 805–812, https://doi.org/10.3189/002214310794457209, 2010.

15 Mainprice, D., Bachmann, F., Hielscher, R., and Schaeben, H.: Descriptive tools for the analysis of texture projects with large datasets using MTEX: strength, symmetry and components, Geological Society, London, Special Publications, 409, SP409–8, 2014.

Mansuy, P., Philip, A., and Meyssonnier, J.: Identification of strain heterogeneities arising during deformation of ice, Annals of Glaciology, 30, 121–126, https://doi.org/10.3189/172756400781820651, 2000.

Martín, C., Gudmundsson, G. H., Pritchard, H. D., and Gagliardini, O.: On the effects of anisotropic rheology on ice flow, internal structure,
20 and the age-depth relationship at ice divides, Journal of Geophysical Research: Earth Surface, 114, https://doi.org/10.1029/2008JF001204, 2009.

Montagnat, M., Blackford, J. R., Piazolo, S., Arnaud, L., and Lebensohn, R. A.: Measurements and full-field predictions of deformation heterogeneities in ice, Earth and Planetary Science Letters, 305, 153–160, https://doi.org/10.1016/j.epsl.2011.02.050, 2011.

Montagnat, M., Castelnau, O., Bons, P. D., Faria, S. H., Gagliardini, O., Gillet-Chaulet, F., Grennerat, F., Griera, A., Lebensohn, R. A.,
25 Moulinec, H., Roessiger, J., and Suquet, P.: Multiscale modeling of ice deformation behavior, Journal of Structural Geology, 61, 78–108, https://doi.org/10.1016/j.jsg.2013.05.002, 2014.

Montagnat, M., Chauve, T., Barou, F., Tommasi, A., Beausir, B., and Fressengeas, C.: Analysis of Dynamic Recrystallization of Ice from EBSD Orientation Mapping, Frontiers in Earth Sciences, 2015.

Paterson, M. S. and Olgaard, D. L.: Rock deformation tests to large shear strains in torsion, Journal of Structural Geology, 22, 1341–1358,
30 https://doi.org/10.1016/S0191-8141(00)00042-0, 2000.

Peternell, M., Russell-Head, D., and Wilson, C.: A technique for recording polycrystalline structure and orientation during in situ deformation cycles of rock analogues using an automated fabric analyser, Journal of Microscopy, 242, 181–188, https://doi.org/10.1111/j.1365-2818.2010.03456.x, 2011.

Piazolo, S., Montagnat, M., and Blackford, J. R.: Sub-structure characterization of experimentally and naturally deformed ice using cryo-
35 EBSD, Journal of Microscopy, 230, 509–519, https://doi.org/10.1111/j.1365-2818.2008.02014.x, 2008.

Piazolo, S., Montagnat, M., Grennerat, F., Moulinec, H., and Wheeler, J.: Effect of local stress heterogeneities on dislocation fields: Examples from transient creep in polycrystalline ice, Acta Materialia, 90, 303–309, https://doi.org/10.1016/j.actamat.2015.02.046, 2015.

Randle, V.: Microtexture determination and its applications, The Institute of Materials(UK), p. 174, 1992.

Russell-Head, D. S. and Wilson, C. J. L.: Automated fabric analyser system for quartz and ice, Geological Society of Australia Abstracts, 64, 159–159, 1999.

Signorelli, J. and Tommasi, A.: Modeling the effect of subgrain rotation recrystallization on the evolution of olivine crystal preferred orientations in simple shear, Earth and Planetary Science Letters, 430, 356–366, https://doi.org/10.1016/j.epsl.2015.08.018, 2015.

5   Thorsteinsson, T. and Waddington, E. D.: Folding in strongly anisotropic layers near ice-sheet centers, Annals of Glaciology, 35, 480–486, https://doi.org/10.3189/172756402781816708, 2002.

Tommasi, A. and Vauchez, A.: Heterogeneity and anisotropy in the lithospheric mantle, Tectonophysics, 661, 11–37, https://doi.org/10.1016/j.tecto.2015.07.026, 2015.

Tommasi, A., Knoll, M., Vauchez, A., Signorelli, J. W., Thoraval, C., and Logé, R.: Structural reactivation in plate tectonics controlled by
10   olivine crystal anisotropy, Nature Geoscience, 2, 423–427, https://doi.org/10.1038/ngeo528, 2009.

Weikusat, I., Miyamoto, A., Faria, S. H., Kipfstuhl, S., Azuma, N., and Hondoh, T.: Subgrain boundaries in Antarctic ice quantified by X-ray Laue diffraction, Journal of Glaciology, 57, 111–120, https://doi.org/10.3189/002214311795306628, 2011.

Wenk, H.-R. and Tomé, C. N.: Modeling dynamic recrystallization of olivine aggregates deformed in simple shear, Journal of Geophysical Research: Solid Earth, 104, 25 513–25 527, https://doi.org/10.1029/1999JB900261, 1999.

15   Wenk, H. R., Canova, G., Bréchet, Y., and Flandin, L.: A deformation-based model for recrystallization of anisotropic materials, Acta Materialia, 45, 3283–3296, https://doi.org/10.1016/S1359-6454(96)00409-0, 1997.

Wheeler, J., Mariani, E., Piazolo, S., Prior, D., Trimby, P., and Drury, M.: The weighted Burgers vector: a new quantity for constraining dislocation densities and types using electron backscatter diffraction on 2D sections through crystalline materials, Journal of Microscopy, 233, 482–494, https://doi.org/10.1111/j.1365-2818.2009.03136.x, 2009.

20   Wilson, C. J., Luzin, V., Piazolo, S., Peternell, M., and Hammes, D.: Experimental deformation of deuterated ice in 3D and 2D: identification of grain-scale processes, Proceedings of the Royal Society of Victoria, 127, 99–104, http://www.publish.csiro.au/paper/RS15011, 2015.

Wilson, C. J. L., Burg, J. P., and Mitchell, J. C.: The origin of kinks in polycrystalline ice, Tectonophysics, 127, 27–48, https://doi.org/10.1016/0040-1951(86)90077-6, 1986.

Wright, S. I., Nowell, M. M., and Field, D. P.: A review of strain analysis using electron backscatter diffraction, Microscopy and Microanaly-
25   sis: The Official Journal of Microscopy Society of America, Microbeam Analysis Society, Microscopical Society of Canada, 17, 316–329, https://doi.org/10.1017/S1431927611000055, 2011.

Table 1. Torsion experiments details for each samples. The sample that was annealed is indicated with an asterisk.

Sample	radius (mm)	height (mm)	$M_{max}(N.m)$	τ_{max} (MPa)	ε_{max}	Duration (h)	$\dot{\gamma}_f$ (s^{-1})	$\dot{\varepsilon}_f$ (s^{-1})
TGI0.012	19.15	56.05	5.8	0.4	0.006	23	$1.6 \cdot 10^{-7}$	$0.8 \cdot 10^{-7}$
TGI0.2	17.70	68.50	4.9	0.5	0.1	210	$5.3 \cdot 10^{-7}$	$2.7 \cdot 10^{-7}$
TGI0.42	16.40	57.65	4.8	0.6	0.21	270	$1.1 \cdot 10^{-6}$	$5.3 \cdot 10^{-7}$
TGI1.96	16.25	52.20	4.9	0.6	0.87	430	$2.1 \cdot 10^{-6}$	$8.6 \cdot 10^{-7}$
TGI0.71*	16.10	59.9	4.0	0.5	0.35	310	$1.8 \cdot 10^{-6}$	$8.4 \cdot 10^{-7}$

The Cryosphere
Discussions

Table 2. Grain size and shape analysis results based on AITA measurements. The sample that was annealed is indicated by an asterisk. n_g is the number of grains used for the analyses and d_g the median of the grain size (with associated interquartile range). Standard deviations are indicated in parentheses.

Sample	n_g	d_g (mm)	PARIS factor (%)
Unstrained	558	0.7(4)	2.2(1.3)
TGI0.012	373	0.4(2)	1.9(1.5)
TGI0.2	1112	0.14(17)	9.6(12.8)
TGI0.42	679	0.4(4)	11.5(15.2)
TGI1.96	926	0.12(16)	5.9(8.4)
TGI0.71*	176	1.7(2.4)	4.9(6.3)

Open Access

Discussions